The Astrophysical Journal, 936:83 (9pp), 2022 September 1 https://doi.org/10.3847/1538-4357/ac8873
© 2022. The Author(s). Published by the American Astronomical Society.
OPEN ACCESS

Manifestation of Gravitational Settling in Coronal Mass Ejections Measured in the Heliosphere

Yeimy J. Rivera[1], John C. Raymond[1], Enrico Landi[2], Susan T. Lepri[2], Katharine K. Reeves[1], Michael L. Stevens[1], and B. L. Alterman[3]
[1] Harvard-Smithsonian Center for Astrophysics, 60 Garden Street, Cambridge, MA 02138, USA
[2] University of Michigan Department of Climate & Space Sciences & Engineering 2455 Hayward Street, Ann Arbor, MI 48109-2143, USA
[3] Space Science and Engineering, Southwest Research Institute, 6220 Culebra Road, San Antonio, TX 78238, USA
Received 2022 April 28; revised 2022 July 3; accepted 2022 August 8; published 2022 September 1

Abstract

Elemental composition in the solar wind reflects the fractionation processes at the Sun. In coronal mass ejections (CMEs) measured in the heliosphere, the elemental composition can vary between plasma of high and low ionization states as indicated by the average Fe charge state, $\langle Q_{Fe} \rangle$. It is found that CMEs with higher ionized plasma, $\langle Q_{Fe} \rangle$ greater than 12, are significantly more enriched in low first ionization potential (FIP) elements compared to their less ionized, $\langle Q_{Fe} \rangle$ less than 12, counterparts. In addition, the CME elemental composition has been shown to vary along the solar cycle. However, the processes driving changes in elemental composition in the plasma are not well understood. To gain insight into this variation, this work investigates the effects of gravitational settling in the ejecta to examine how that process can modify signatures of the FIP effect found in CMEs. We examine the absolute abundances of C, N, O, Ne, Mg, Si, S, and Fe in CMEs between 1998 and 2011. Results show that the ejecta exhibits some gravitational settling effects in approximately 33% of all CME periods in plasma where the Fe abundance of the ejecta compared to the solar wind (Fe/H_{CME}:Fe/H_{SW}) is depleted compared to the C abundance (C/H_{CME}:C/H_{SW}). We also find gravitational settling is most prominent in CMEs during solar minimum; however, it occurs throughout the solar cycle. This study indicates that gravitational settling, along with the FIP effect, can become important in governing the compositional makeup of CME source regions.

Unified Astronomy Thesaurus concepts: Solar coronal mass ejections (310); Chemical abundances (224); Solar cycle (1487); Solar coronal transients (312)

1. Introduction

Spatial and temporal variations in the chemical composition at the Sun and in the heliosphere have long been observed (Pottasch 1963). Several studies reveal that plasma composition can depend on the element's first ionization potential (FIP), mass, and mass per charge squared, which act through the interplay of the FIP effect, gravitational settling, and Coulomb drag processes, respectively, operating between the chromosphere and corona (Geiss 1982; Feldman & Widing 1992; Bodmer & Bochsler 2000). However, the conditions that determine the dominating driver of changes in elemental composition for different solar structures can be unclear.

Studies of coronal loop structures have indicated that gravitational settling effects can appear in large, long-lived coronal loops (Lenz et al. 1998). In this scenario, plasma in coronal loops can undergo diffusion and gravitational effects that can fractionate plasma according to elemental mass, depleting heavier ion densities high in the corona. Lenz et al. (1998) found the gravitational stratification timescale in coronal loops to be on the order of 1 day and strongly governed by the thermodynamic structure of the loop. Observations of large helmet streamers have also strongly indicated gravitational settling effects appearing at the core of quiescent streamers that form above quiescent filaments or quiet Sun at heights between 1.5 and $6R_{\odot}$ (Raymond et al. 1997a, 1997b, 1998; Raymond 1999). Spectral observations from SOHO/UVCS show significant depletion of both low (FIP < 10 eV) and high (FIP > 10 eV) FIP elements (O, Si, and Mg) at the core or center of quiescent streamers thought to be caused by gravitational stratification (Uzzo et al. 2003, 2004), although the FIP effect was present as well showing both processes can occur in the same structure.

Additionally, remote observations of gravitational settled plasma show a strong spatial dependence where the elemental depletion is most prominent at the streamer *core*, mainly in closed magnetic field topology, and gradually disappears at the edge of the loop where the plasma lies on a mixture of closed and open field lines. In line with these results, the intensity falloff in equatorial streamers occurs faster for lines of Fe as compared to those of lighter elements (Ne, Mg, and Si) indicating strong gravitational effects as a function of altitude along the streamer structure as well (Feldman et al. 1998).

Moreover, evidence of compositionally depleted periods in the slow solar wind has been observed in situ (Weberg et al. 2012, 2015). Weberg et al. (2012) investigated periods of anomalous depletion in the absolute abundance of Fe, Fe/H. Apart from Fe, these periods were found to be depleted of several other elements in accordance with particle mass. The mass-fractionated periods in Weberg et al. (2012) were thought to be the in situ manifestations of material from coronal loops like those observed with SOHO/UVCS at the Sun.

Unlike gravitational settling effects that appear less frequently in the solar wind, the FIP effect is a main feature of the solar wind and in CMEs in the heliosphere and has been

Original content from this work may be used under the terms of the Creative Commons Attribution 4.0 licence. Any further distribution of this work must maintain attribution to the author(s) and the title of the work, journal citation and DOI.

studied extensively with heavy ion measurements (von Steiger et al. 2000; Zurbuchen et al. 2016). For instance, through the Ulysses mission, in and out of the ecliptic measurements of heavy ions revealed fundamental differences in the chemical composition between polar coronal holes and equatorial wind from streamer structures. Several polar passes revealed that traditional *fast* coronal hole solar wind contains an elemental composition more closely related to the photosphere of the Sun while the *slow* equatorial solar wind appeared more compositionally variable. In CMEs, Zurbuchen et al. (2016) found the ejecta contained elevated low FIP elements (Mg, Fe, and Si) and mid-FIP S and high-FIP Ne compared to all solar wind. In fact, this study also indicated that not all CMEs are equally enhanced. The study found higher ionized CMEs, those with an average Fe charge state, $\langle Q_{\rm Fe}\rangle$, greater than 12, to be significantly more low FIP enhanced and enhanced in S, Ne compared to less ionized CMEs, those with a $\langle Q_{\rm Fe}\rangle$ less than 12. This suggests a fundamental difference in elemental makeup of CME plasma of higher versus lower ionized material that may be FIP independent. Furthermore, several other studies have reported significant depletion of individual ions, those fully stripped of electrons, which can also be a factor in the overall chemical composition observed in CME structures (Kocher et al. 2017; Rivera et al. 2021). However, it remains unclear what drives the changes observed across CME structures.

In CMEs and the solar wind, $\langle {\rm Q_{Fe}}\rangle$, similar to O^{7+}/O^{6+} and C^{6+}/C^{5+}, measured in situ is frequently used to categorize plasma source regions because they are a direct reflection of the thermodynamic evolution experienced between the plasma's source region and acceleration into the interplanetary medium (Lepri et al. 2001; Goryaev et al. 2020). On the other hand, the elemental composition is set prior to the eruption through the interplay of the FIP effect and gravitational settling, enabling us to probe processes connected to its source region. It is important to explore the relationship between elemental and ion composition to understand the plasma's source region in connection with the conditions experienced during its release and evolution from the eruption site into interplanetary space.

In this work, we aim to understand the importance of gravitational settling effects in CME plasma as well as how that impacts the FIP bias and the overall composition of the ejecta and source region. We investigate the effect of gravitational settling in CMEs measured at 1 au across solar cycle 23 by examining the heavy elemental composition compared to the solar wind to determine if changes in the plasma exhibit mass fractionation. We investigate the compositional variation across a range of $\langle Q_{\rm Fe}\rangle$ in CME periods at 1 au to understand the relationship between elemental composition and the plasma's ionization state. This paper is organized as follows: Section 2 describes the observations from ACE/SWICS. Section 3 presents the results showing gravitational settling features in the composition of CMEs. Section 4 discusses the impact of gravitational settling effects on elemental composition and its source region. Section 5 summarizes the main results.

2. Observations

We use ion composition data from the Solar Wind Ion Composition Spectrometer (SWICS; Gloeckler & Geiss 1992), and proton measurements from the Solar Wind Electron, Proton, and Alpha Monitor (SWEPAM; McComas et al. 1998) on the Advanced Composition Explorer (ACE) to identify evidence of gravitational settling inside CMEs. SWICS is made up of an electrostatic analyzer (ESA) with an energy-resolving time-of-flight (TOF) instrument to measure the heavy ion composition of the solar wind. The combination of an ESA paired with a TOF telescope enables the identification and characterization of individual ions using each particle's energy per charge (E/Q), TOF, and total energy, E. These three measurements allow for the identification of a large range of ions of He, C, N, O, Ne, Mg, Si, S, and Fe, in the E/Q range of 0.49–60 keV e^{-1}. We use 2 hr integrated time measurements, which produce the best quality observations, with an accuracy of better than 20%. We note that for the composition of Ne, we do not include ion densities of Ne^{6+} and Ne^{7+}, which cannot reliably be measured with SWICS since those counts are largely overwhelmed by the $O^{5,6+}$ signal. Simulations of the fast speed wind show that the $Ne^{6,7+}$ contribution is roughly ~15% in coronal hole wind and becomes less significant in slower speed solar wind (Landi et al. 2012). The $\langle {\rm Q_{Fe}}\rangle$ of coronal hole solar wind ($V_p > 500\,{\rm km\,s^{-1}}$) is 9.26 ± 1.3; therefore, in the present study, Ne/H can include an additional uncertainty as high as 15% for $\langle {\rm Q_{Fe}}\rangle$ less than 10.5.

The CME boundaries in the in situ measurements in this study are selected using the list from Richardson & Cane (2010) which has been expanded using the online list.[4] The list is curated using several in situ CME plasma, magnetic field, and energetic particle signatures. These include enhancement of proton density, velocity, temperature, and magnetic field during the passage of the CME shock front, followed by low proton density and temperature across the CME body indicating rapid expansion, high $\langle {\rm Q_{Fe}}\rangle$, O^{7+}/O^{6+}, and C^{6+}/C^{5+} values associated with significant heating during the eruption, and counter-streaming electrons signatures indicating the passage of a magnetic flux rope rooted at the Sun on one or both ends. Further details on the observational characteristics of CMEs in the heliosphere can be found in Cane & Richardson (2003), Zurbuchen & Richardson (2006), and Richardson & Cane (2010). In this work, we also include measurements from a 6 hr buffer after each CME to cover the trailing ejecta that can often extend outside of the Richardson & Cane CME boundaries in charge states measurements (Richardson & Cane 2010) and to account for previous studies that find differences between CME boundaries (Jian et al. 2006; Anderson et al. 2012).

3. Analysis and Results

We investigated the composition of heavy elements in CMEs across solar cycle 23 to determine if gravitational settling is reflected in the compositional makeup of the ejecta. The observations include all periods inside CME boundaries including the sheath, flux rope, and prominence material. Traditionally, in situ observations of elemental composition in the solar wind and transients are normalized to oxygen (von Steiger et al. 2000; Zurbuchen et al. 2002, 2003); however, to remove any effects from gravitational settling exhibited by O, we use absolute abundances where the elemental composition is normalized to the proton density, H. Using absolute abundances, X/H, will enable us to capture the variation of heavy ions to study gravitational effects more clearly. This comparison has been done previously in Weberg et al. (2012)

[4] http://www.srl.caltech.edu/ACE/ASC/DATA/level3/CMEtable2.htm

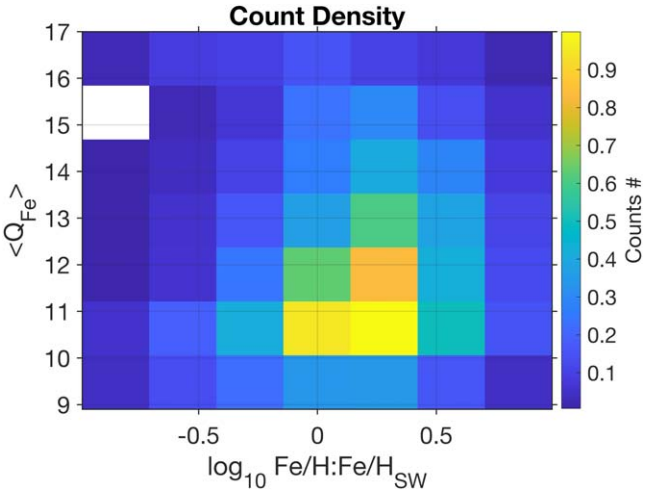

Figure 1. (Top) Plot of the normalized counts of CME periods across different Fe absolute abundances compared to the solar wind, as $\log_{10}$ Fe/H:Fe/H_{SW} and $\langle Q_{Fe}\rangle$. The color bar indicates counts normalized to the peak of the distributions of 2 hr integrated measurements of CMEs between 1998 and 2011.

in the solar wind and in Lepri & Rivera (2021) for prominence material in CMEs for the same purpose.

Similar to Weberg et al. (2012) in the solar wind, we examined changes in the absolute abundances, X/H, of CME plasma from the distributions of 2 hr integrated periods inside CMEs. For a more detailed view, we have plotted the absolute abundance that is organized by the average Fe charge state, $\langle Q_{Fe}\rangle$, and the ratio of Fe absolute abundances between CME plasma and the solar wind, as $\log_{10}$Fe/H:Fe/H_{SW} as shown in Figure 1. The Fe/H_{SW} values are from the solar wind speed $V_p < 400\ \mathrm{km\ s^{-1}}$ during the entire data set between 1998 and 2011 where no depleted periods were found. The reason for selecting the slow solar wind was to remain consistent with the work of Weberg et al. (2012, 2015) where the solar wind-depleted periods were compared with the non-depleted surrounding slow solar wind. Additionally, a comparison between CMEs to fast solar wind or photospheric composition shows significant low-FIP enhancements that completely dominate the compositional signature, overwhelming any mass-proportional dependence. The figure shows a 2D histogram of the CME plasma distribution of specific $\langle Q_{Fe}\rangle$ across values of Fe/H that are depleted or enhanced compared to the solar wind to examine plasma of high and low Fe abundances. The figure indicates that the majority of CME plasma lies within $\langle Q_{Fe}\rangle = 9.5$–13 and Fe/H:Fe/$H_{SW}$ ranges between 1 and 3.

The plots shown in Figure 2 are 2D histograms, similar to the plot in Figure 1, showing the ratio of the absolute abundance of CME to solar wind plasma, $\log_{10}$ X/H:X/H_{SW}, for each element across $\langle Q_{Fe}\rangle$ and $\log_{10}$Fe/H:Fe/H_{SW} space. Each bin is a mean value for all plasma periods within that bin. The histograms are organized by particle mass from lightest to heaviest as C, N, O, Ne, Mg, Si, S, and Fe. From the histograms, we observe a general enhancement of X/H:X/H_{SW} with increasing Fe abundance that appears nearly independent of $\langle Q_{Fe}\rangle$. However, C, N, and O show larger enhancement in the lower right of the plot, at low $\langle Q_{Fe}\rangle$ and $\log_{10}$ Fe/H:Fe/H_{SW} between 0 and 0.5, while Ne, Mg, and to a lesser extent S show an enrichment at the top right of the distribution, where $\langle Q_{Fe}\rangle$ and Fe/H:Fe/H_{SW} are high.

To examine X/H:X/H_{SW} across $\langle Q_{Fe}\rangle$ in more detail, in Figure 3 we plot the normalized $\log_{10}$ X/H:X/H_{SW} with increasing $\langle Q_{Fe}\rangle$ for each Fe/H:Fe/H_{SW} bin, i.e., a plot of each column of bins from Figure 2. The figure shows a change in trends between depleted (blue to green) and enhanced (red to yellow) values of Fe/H:Fe/H_{SW} plasma across particle mass. The lightest elements (C, N, and O) show a decline of X/H:X/H_{SW} as Fe ionization increases in Fe-enhanced plasma with the exception of the dark red bin of 0.846. Conversely, the opposite trend is observed for Fe-depleted plasma, which increases toward high $\langle Q_{Fe}\rangle$ to a value near 1 for bins −0.566 and −0.284. For Ne and S, and to a lesser extent Mg and Si, their X/H:X/H_{SW} values gradually increase with increasing $\langle Q_{Fe}\rangle$ in both Fe-enriched and depleted plasma, showing similar behavior. As will be discussed in Section 4, the variation across different Fe/H:Fe/H_{SW} values is likely due to the interplay of gravitational settling and the FIP effect both becoming important in regulating the elemental composition in the CME source region.

To examine the overall plasma behavior across particle mass of high and low Fe/H abundance periods, we classify each 2 hr integrated CME period between the plasma of Fe/H:Fe/H_{SW}, which is lower and higher than C/H:C/H_{SW}. The two classifications are intended to identify when CME plasma is significantly depleted of Fe (C/H:C/H_{SW} > Fe/H:Fe/H_{SW}) suggesting strong gravitational settling is present while cases where Fe/H:Fe/H_{SW} > C/H:C/H_{SW} would indicate strong FIP effect features dominate. Figure 4 presents the mean ratio of X/H:X/H_{SW} for different particle mass in each case where C/H:C/H_{SW} is larger (black diamonds) and smaller (red diamonds) than Fe/H:Fe/H_{SW} where the error bars are the standard deviation. The top figure shows the values for all CME periods while the bottom plots show only periods where prominences from Lepri & Rivera (2021) are detected in the CMEs. In the top plot, when comparing the CME plasma of the two populations, we find the plasma with high C/Fe (black diamonds) shows mass-proportional depletion, as the X/H:X/H_{SW} value of each element becomes progressively more depleted with increasing particle mass. This trend suggests that CME plasma where the C/H:C/H_{SW} > Fe/H:Fe/H_{SW} exhibits some mass fractionation. Conversely, the opposite trend is observed in the rest of the CME plasma. For plasma with low C/Fe (red diamonds), C, N, and O appear depleted compared to the solar wind while the remaining elements are enhanced with increasing mass up to Ne and Mg, Si, S, and Fe remain at similar enhancement levels.

When examining only prominence plasma, as shown in the bottom plot of Figure 4, we find that the enhancement in the black diamonds is significantly larger in this subset of plasma compared to the entire data set. The significant heavy ion enhancement found in the present study is in line with results from Lepri & Rivera (2021). The variability and enhancement in the prominence material can also be seen in Figure 5 represented by the stars in panel (a), as is discussed later. Prominence periods constitute only 2% of all periods associated with high C/Fe periods making their overall contribution to the trend observed in the top plot small as well as less statistically significant. We find that the black diamond population resembles the trend observed in the top plot as seen by the sharp decline in X/H:X/H_{SW} values with increasing mass except for Fe, which remains at the same degree of enhancement as Si. This may indicate that these structures

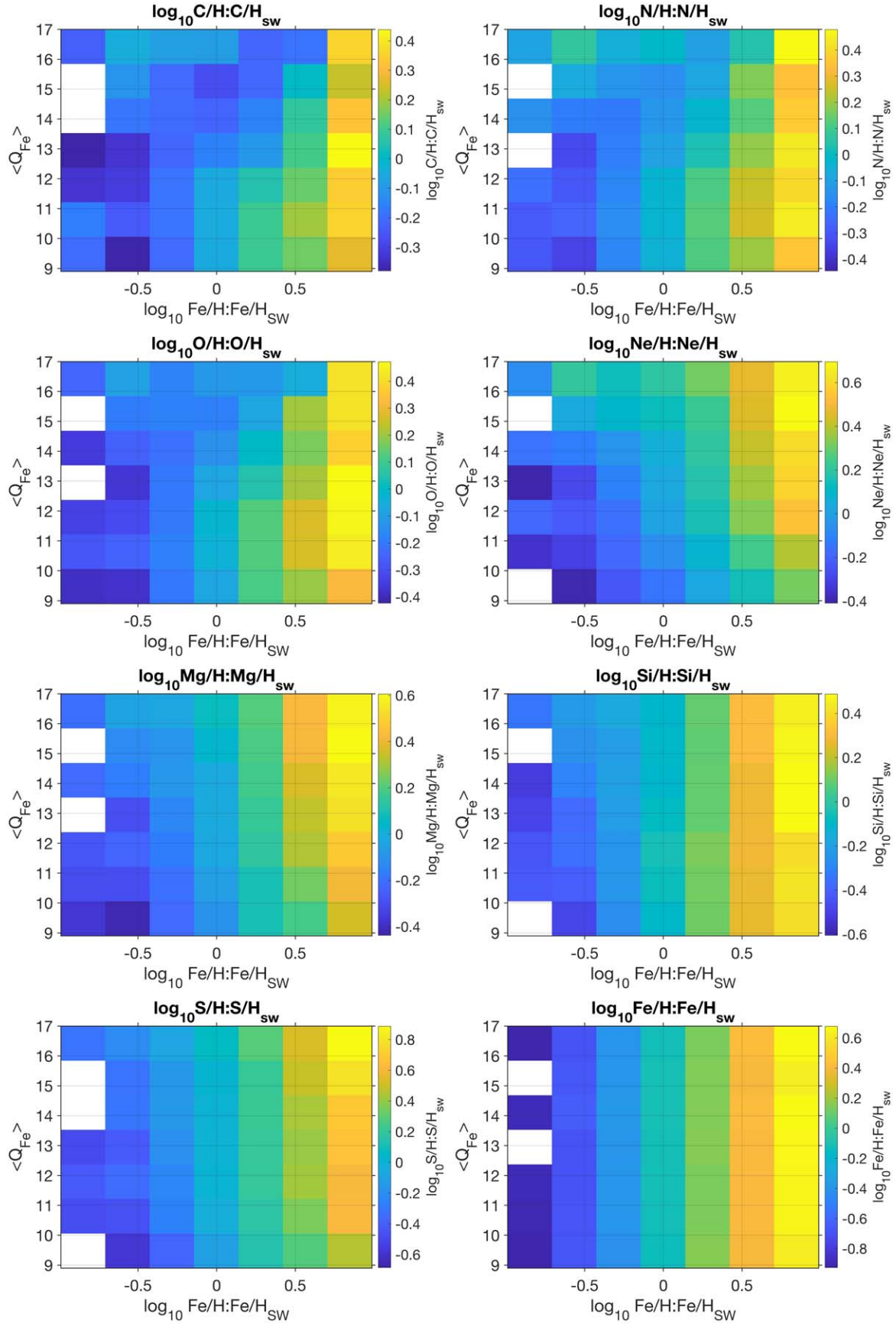

Figure 2. 2D histogram of CME plasma of $\langle Q_{Fe} \rangle = 9$–17 and $\log_{10}$ Fe/H:Fe/H_{SW}. The color bar indicates the value of elemental density, X, divided by the proton density normalized to its solar wind value as $\log_{10}$X/H:X/H_{SW}. The error bars are the standard deviation of the points.

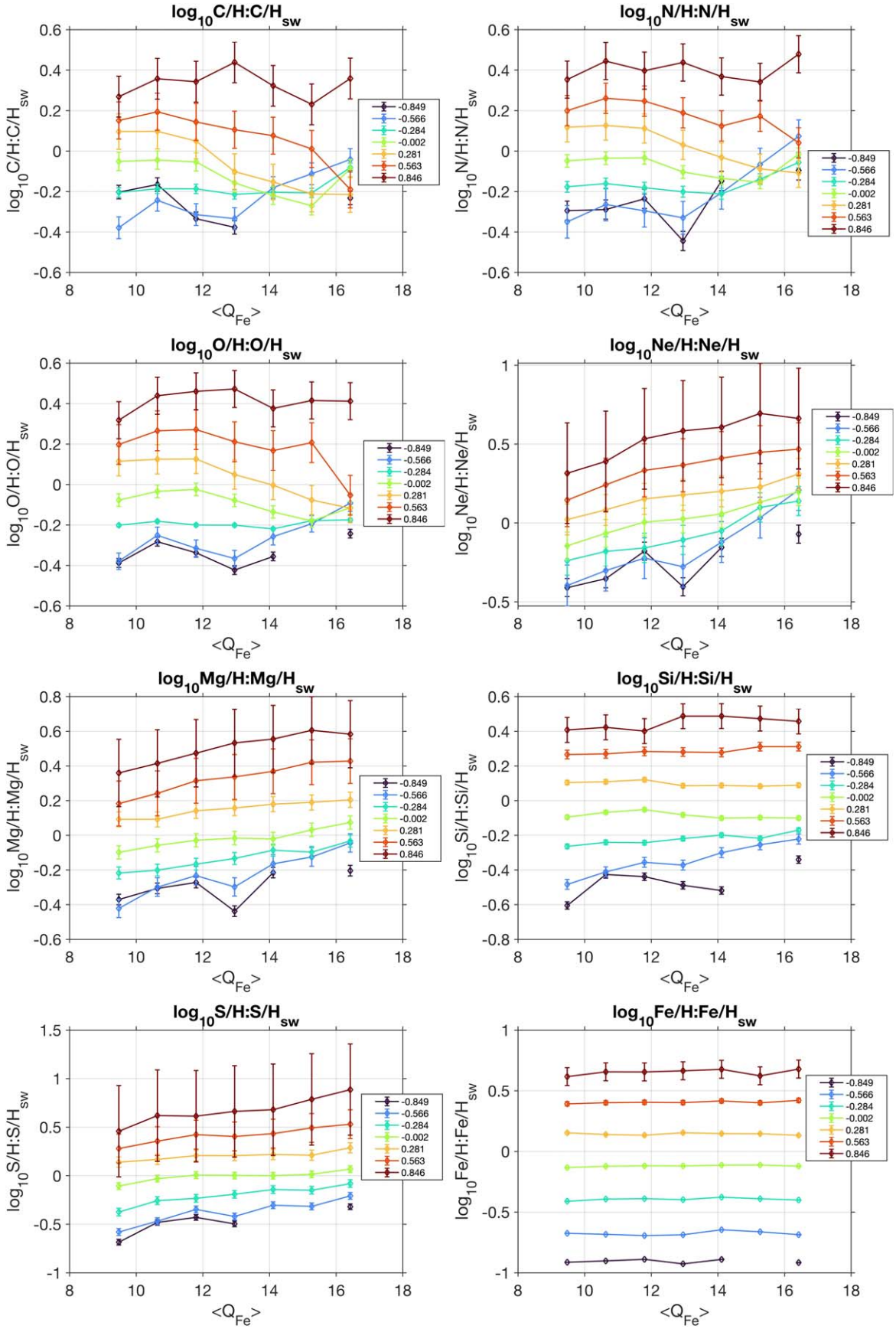

Figure 3. Plots of $\log_{10}$ X/H:X/H_{SW} across $\langle Q_{Fe} \rangle$ for each Fe/H:Fe/H_{SW} bin in Figure 2. The legend indicates the value for each $\log_{10}$ Fe/H:Fe/H_{SW} bin. The error bars are the standard deviation of the points.

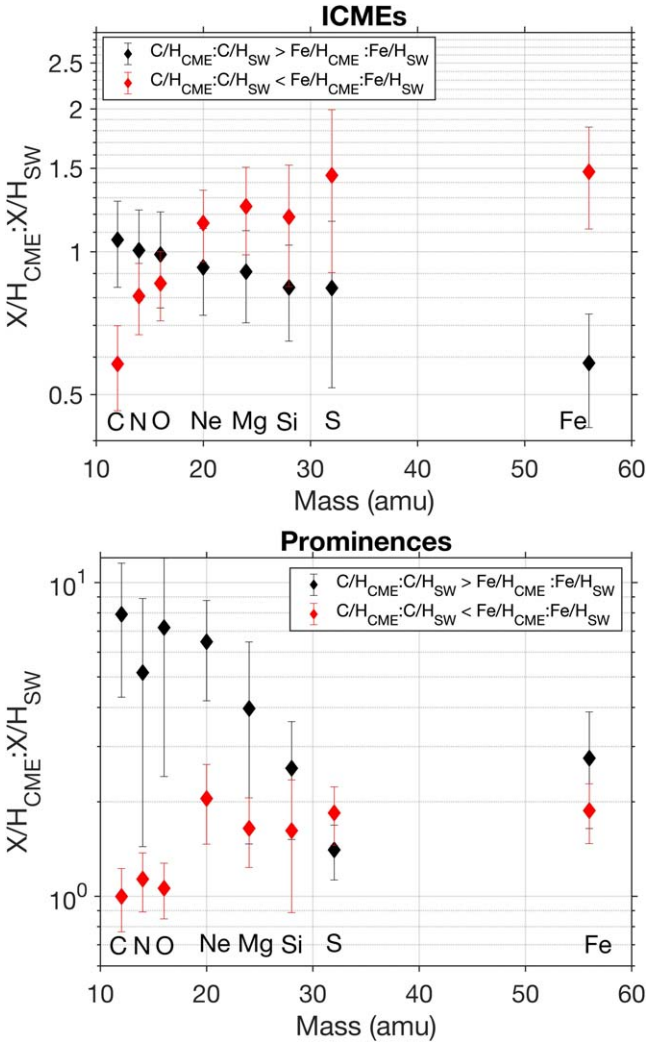

Figure 4. (Top plot) Ratio of each element from interplanetary CMEs divided by proton density, X/H_{CME}, and normalized by the solar wind, X/H_{SW}, for plasma where C/H_{CME}:$C/H_{SW} >$ Fe/H_{CME}:Fe/H_{SW} (black diamonds) and vice versa (red diamonds) organized by mass. The bottom plot is the same for isolated prominences within CMEs as identified in Lepri & Zurbuchen (2010) and Lepri & Rivera (2021).

exhibit mass fractionation, but its signatures are much less clear.

Figure 5 is a multi-panel plot showing an example of two CMEs that exhibit strong mass-fractionation effects. The red solid and dashed vertical lines represent the start and end, respectively, of the CME boundaries. Panel (a) plots the ratio of absolute abundances between the CME and solar wind plasma as $X/H{:}X/H_{SW}$. Panels (b)–(d) show the relative abundances for C, O, and Fe charge state distributions. Panels (e)–(g) show the proton temperature, velocity, and density, respectively. Panel (h) shows the magnetic field magnitude and RTN field components. In panel (a), the solid lines of the different elements represent the ratio across the CME body, while the stars represent a prominence period and the dots represent non-prominence periods for instances with high C/Fe associated with the black diamonds in Figure 4. In the first CME, a prominence is present in the second half of the ejecta where low ionized C, O, and Fe ions are present, as detailed in Lepri & Zurbuchen (2010) and Lepri & Rivera (2021). During this instance, we observe a significant enhancement of heavy ion densities compared to solar wind values with the largest enhancement occurring in lighter elements compared to heavier ones, as summarized for all prominence periods in the bottom plot of Figure 4. In the second CME, there is a sharp decline in the heavy ion ratios toward a value of 1, as shown in panel (a). The periods associated with the black diamonds (dots) show that the elements are generally organized from lightest to heaviest (blue to yellow) where Fe abundances are significantly more depleted than the solar wind, and in certain cases, its abundance becomes too low to be measured, as illustrated by the empty values in panel (d). Since the heaviest particles like Fe, and occasionally S, disappear completely, while the lightest elements like C, N, and O remain close to the solar wind abundances, suggests that heavier elements may be preferentially depleted.

Moreover, we find the periods associated with high C/Fe constitute approximately 33% of all CME periods across the solar cycle, as shown in Figure 6. In the figure, the left plot shows the number of 2 hr periods for all CMEs (blue), for the cases of high C/Fe (black), along with the sunspot number (red curve) across 1998–2012. Moreover, the right plot of the same figure shows the ratio of the periods in black to all the CME periods in blue of the left plot, showing a slight solar cycle dependence. The plot shows a larger percentage of CMEs periods including instances with high C/Fe during solar minimum compared to solar maximum, indicating that a larger fraction of the ejecta could be originating from mass-fractionation plasma at the Sun.

Lastly, it is found that mass-fractionated plasma that is associated with high C/Fe tends to have lower $\langle Q_{Fe} \rangle$ plasma. Figure 7 illustrates the normalized distribution of $\langle Q_{Fe} \rangle$ values of the two populations, showing that periods where $C/H{:}C/H_{SW} >$ $Fe/H{:}Fe/H_{SW}$ are more frequently associated with less ionized CMEs structures while a larger fraction of the rest is found in structures that are significantly more ionized and heated.

4. Discussion

Through the comparison of the elemental composition of all CME plasma and the solar wind, we find gravitational settling may be present in the substructure of CMEs. The gravitational settling arises in some parts of the CME as the mass-proportional depletion of its abundance compared to the solar wind shown in the black diamonds of the top plot in Figure 4. Conversely, the remaining CME plasma (red diamonds) is enhanced compared to the solar wind abundance, except for C, N, and O, and shows some dependence on particle mass in the lightest elements (C, N, O, and Ne) only. This suggests that only some structures that make up the CME body exhibit significant gravitational settling effects.

The CME structures associated with the mass-fractionated plasma could have originated from large coronal loops formed above the AR that are ejected during the eruption. As indicated from several helmet streamer observations taken by SOHO/UVCS, AR helmet streamers can exhibit gravitational stratification in line with observations in this study and previous work in the solar wind (Raymond et al. 1997b; Uzzo et al. 2003, 2004; Weberg et al. 2012). As shown in Figure 8, we find good agreement between the majority of absolute abundances computed for a mass-stratified streamer core and leg (orange and yellow squares, respectively) examined in Raymond et al. (1997b) and mass-stratified solar wind

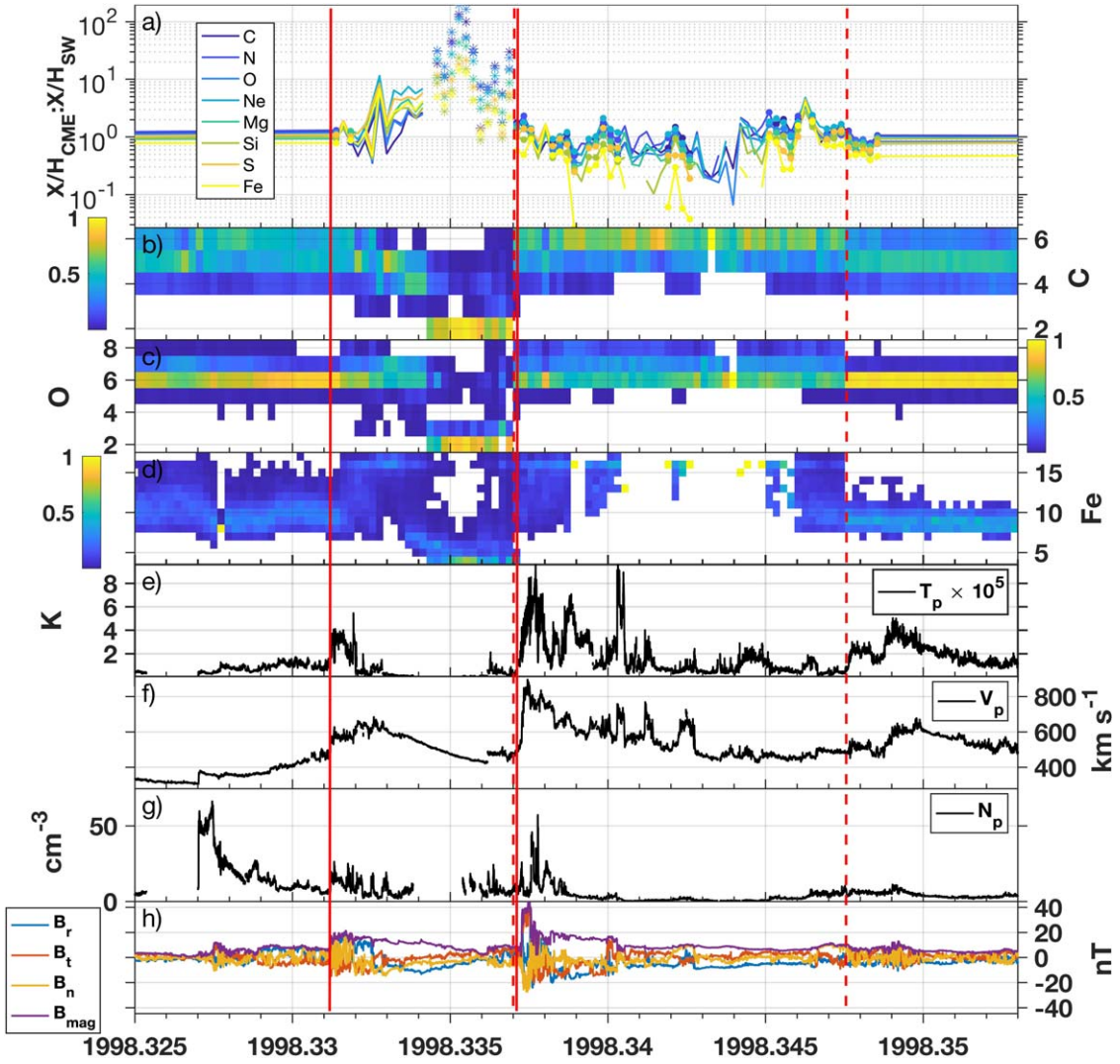

Figure 5. Example of two CMEs as indicated by the solid (start) and dashed (end) vertical lines. The multi-panel shows data from ACE/SWICS, ACE/SWEPAM, and ACE/MAG ranging between days of year 110 and 130. Panel (a) shows the ratio of each element as $X/H{:}X/H_{SW}$ as described in the text. Panels (b)–(d) show the relative abundances of C, O, and Fe, respectively. Panel (e)–(g) show the proton temperature, velocity, and density, respectively. Panel (h) shows the magnetic field magnitude and RTN components.

abundances (blue triangles) from Weberg et al. (2012) compared to the high C/Fe periods in CMEs where mass fractionation is present. This agreement suggests that the dropouts in the solar wind from Weberg et al. (2012) and at the Sun may be connected to the source region of the CMEs depleted periods in the present study. Also shown in the figure, the majority of cases of high C/Fe CME plasma (black diamonds) is depleted of all elemental abundances compared to the typical coronal abundances (purple squares) further suggesting an FIP-independent change to the chemical composition of their source region. Furthermore, we note that the difference in Ne abundance between the streamer and in situ observations is the result of the Ne abundance in the streamer (yellow and orange squares) being an upper limit and having a large uncertainty given the line's strong temperature dependence, as indicated in Raymond et al. (1997b).

Compared to the average gravitational settling effects found in the solar wind, CME plasma shows a smaller degree of relative mass-dependent fractionation. Weberg et al. (2012) report that Fe in the solar wind dropout events was depleted by an average value of 86% as compared to the surrounding solar wind. This value is much larger compared to what is found in CMEs, with a global relative depletion of ∼40%, as shown by the black diamonds in Figure 4. The significant difference could be by virtue of CMEs being highly structured, containing a mixture of sheath material from the neighboring coronal plasma, a magnetic cloud, prominence material, and solar wind of different ion and elemental compositional properties (Richardson & Cane 2010; Owens 2018; Rivera et al. 2019). The combination of these structures can dilute the overall gravitational settling observed in situ compared to those identified purely in the solar wind.

Moreover, our work shows that a larger percentage of the ejecta exhibits gravitational settling during solar minimum compared to solar maximum, as shown in Figure 6. This trend could arise from a more significant contribution of the ejecta being made up of the AR structure at solar maximum. The AR-originating plasma observed in situ could contribute additional non-mass-stratified plasma in solar maximum compared to those ejected in solar minimum.

Furthermore, Figure 9 shows the FIP bias of the two populations in Figure 4 as $X/O{:}X/O_{phot}$ where X/O is the

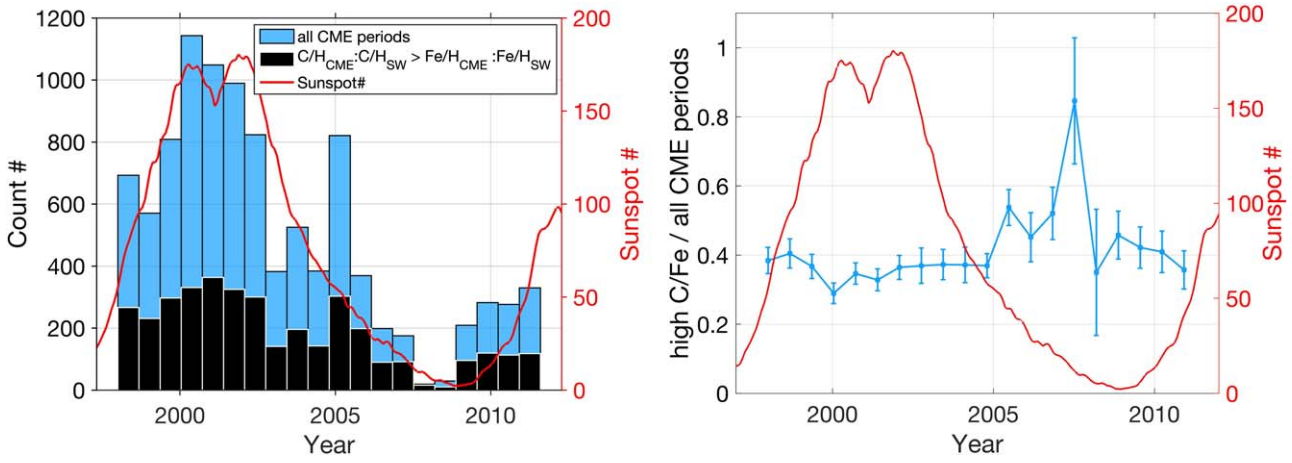

Figure 6. (Left plot) Count distribution of all 2 hr CME periods across the solar cycle in blue, periods associated with the black diamonds in Figure 4 in black, and the red curve is the sunspot number. The right plot shows the ratio of the black to blue distributions from the left plot and the sunspot number in red and the error bars are the Poisson counting statistics uncertainties.

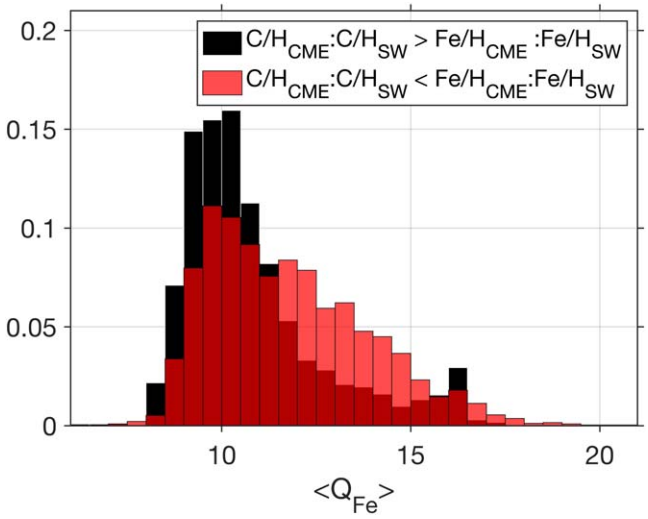

Figure 7. Normalized distribution of the $\langle Q_{Fe} \rangle$ values of the black and red diamond CME periods shown in Figure 4.

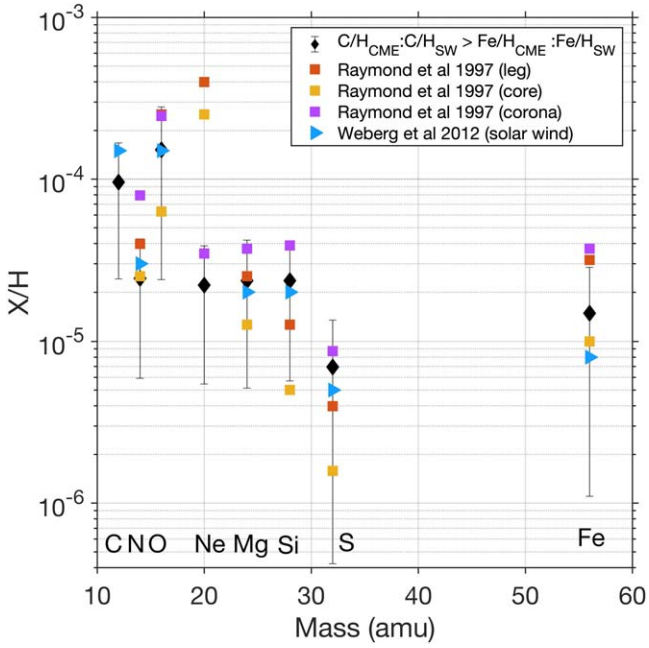

Figure 8. Plot showing the absolute abundance of each element, X/H, organized by mass for the high C/Fe CME plasma population shown in the black diamonds of Figure 4 from this work as compared to the abundances computed for a depleted streamer core and leg, and typical coronal abundances from SOHO/UVCS in Raymond et al. (1997b), and the solar wind depleted periods from Weberg et al. (2012).

CME elemental composition normalized to the photospheric abundance of the same ratio from Asplund et al. (2021). This ratio is traditionally taken to examine the FIP effect in the solar wind and will allow the present analysis to be directly compared to previous observations of CME composition (Zurbuchen & Richardson 2006; Richardson & Cane 2010). $X/O:X/O_{phot}$ will show the enhancement or depletion of the CME plasma composition compared to typical photospheric composition determined from solar models and spectroscopic observations (Asplund et al. 2009, 2021). As shown in Figure 9, we find that CME plasma remains low FIP enhanced in both populations; however, the red diamonds represent significantly higher FIP bias values. This indicates that, in the CME source region connected to the high C/Fe population, both the FIP effect and gravitational processes may be significant and can be important in regulating the chemical makeup of the ejected material. Whereas for low C/Fe plasma, gravitational settling may not be as important, or likely absent, and the FIP effect is more extreme.

Moreover, given that the mass-fractionated CME structures are associated with lower $\langle Q_{Fe} \rangle$ plasma compared to the rest of the CME suggests that, overall, lower $\langle Q_{Fe} \rangle$ CMEs are generally less low FIP enhanced compared to its higher $\langle Q_{Fe} \rangle$ counterpart. This could explain the difference in the FIP bias between *high* ($\langle Q_{Fe} \rangle$ larger than 12) and *other* ($\langle Q_{Fe} \rangle$ less than 12) CMEs investigated in Zurbuchen et al. (2016). In Zurbuchen et al. (2016), other $\langle Q_{Fe} \rangle$ CMEs were overall less low FIP enhanced and contained lower S and Ne abundances while exhibiting a slight enhancement in C and N compared to high $\langle Q_{Fe} \rangle$ CMEs. The differences between the high and other CMEs of that study resemble the changes in the FIP bias observed in the red and black diamonds, respectively, shown in Figure 9. We note that our work computes a $\langle Q_{Fe} \rangle$ for each 2 hr interval of CME periods while Zurbuchen et al. (2016) assign a single $\langle Q_{Fe} \rangle$ value for each CME; however, the general trend between the high and other $\langle Q_{Fe} \rangle$ FIP bias is still observed

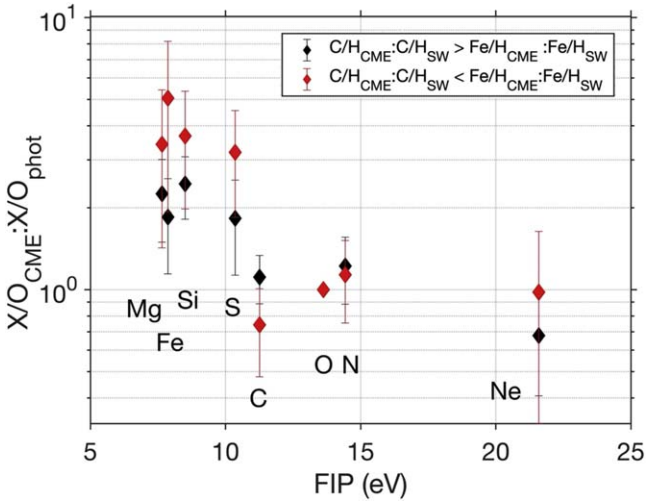

Figure 9. Plot showing the ratio of each element normalized to O and divided by its photospheric value, $X/O{:}X/O_{phot}$, organized by FIP value for the two CME plasma populations in Figure 4.

here. This result strongly suggests that the changes in the FIP bias between CMEs with high and low $\langle Q_{Fe} \rangle$ could be in some part due to gravitational settling effects. This result also suggests that the ejected material from higher in the corona, where gravitational effects are more pronounced, is overall less ionized and heated compared to the material below (Feldman et al. 1998).

5. Conclusions

We investigated the CME elemental composition using ACE/SWICS measurements between 1998 and 2011. Through a comparison of C, N, O, Ne, Mg, Si, S, and Fe abundances with the solar wind, we find that heavy ions in a subset of CME plasma (∼33% of CME periods) are depleted in relation to particle mass where C is least depleted and Fe is most depleted. This effect is most discernible in plasma where the absolute abundance of C in the CME compared to the solar wind, $C/H_{CME}{:}C/H_{SW}$, is larger than that of $Fe/H_{CME}{:}Fe/H_{SW}$. The mass-dependent depletion of heavy elements reaches a mean value of 40% difference between C and Fe. Mass-proportional elemental depletion exhibited in the CME plasma is attributed to gravitational settling occurring in the corona. Furthermore, the degree of overall gravitational settling observed in CME plasma is smaller compared to the values reported in the solar wind (∼86%) by Weberg et al. (2012).

The gravitational settling effects show a slight solar cycle dependence such that CMEs in solar minimum exhibit higher contributions of mass-fractionated plasma compared to those in solar maximum. However, it is unclear if this results from gravitational settling becoming more significant in solar minimum or if the contribution of AR material in solar maximum acts to contribute additional non-mass-stratified plasma. To examine this phenomena further, it is necessary to track the composition of CME source regions across the solar cycle. This will indicate if gravitational settling becomes more pronounced across coronal structures at different phases of the solar cycle.

Y.J.R. acknowledges support from the Future Faculty Leaders postdoctoral fellowship at Harvard University. The work of J.C.R. and K.K.R. was supported by NASA Grant 80NSSC19K0853 to the Smithsonian Institution. B.L.A. acknowledges NASA contract NNG10EK25C. S.T.L. acknowledges support from NASA Grants 80NSSC19K0853, 80NSSC20K0185, 80NSSC18K0645,80NSSC22K0204, and 80NSSC20K0192 to the University of Michigan. E.L. acknowledges support from NASA grants 80NSSC18K0647, 80NSSC18K1553, and 80NSSC20K0185.

ORCID iDs

Yeimy J. Rivera https://orcid.org/0000-0002-8748-2123
John C. Raymond https://orcid.org/0000-0002-7868-1622
Enrico Landi https://orcid.org/0000-0002-9325-9884
Susan T. Lepri https://orcid.org/0000-0003-1611-227X
Katharine K. Reeves https://orcid.org/0000-0002-6903-6832
Michael L. Stevens https://orcid.org/0000-0002-7728-0085
B. L. Alterman https://orcid.org/0000-0001-6673-3432

References

Anderson, B. R., Skoug, R. M., Steinberg, J. T., & McComas, D. J. 2012, JGRA, 117, 4107
Asplund, M., Amarsi, A. M., & Grevesse, N. 2021, A&A, 653, A141
Asplund, M., Grevesse, N., Sauval, A. J., & Scott, P. 2009, ARA&A, 47, 481
Bodmer, R., & Bochsler, P. 2000, JGRE, 105, 47
Cane, H. V., & Richardson, I. G. 2003, JGRA, 108, 1156
Feldman, U., Schuhle, U., Widing, K. G., & Laming, J. M. 1998, ApJ, 505, 999
Feldman, U., & Widing, K. G. 1992, PhyS, 46, 202
Geiss, J. 1982, SSRv, 33, 201
Gloeckler, G., & Geiss, J. 1992, A&A, 92, 267
Goryaev, F. F., Slemzin, V., & Rodkin, D. 2020, ApJ, 905, L17
Jian, L., Russell, C. T., Luhmann, J. G., & Skoug, R. M. 2006, SoPh, 239, 393
Kocher, M., Lepri, S. T., Landi, E., Zhao, L., & Manchester, W. B. 2017, ApJ, 834, 147
Landi, E., Gruesbeck, J. R., Lepri, S. T., & Zurbuchen, T. H. 2012, ApJ, 750, 159
Lenz, D. D., Lou, Y., & Rosner, R. 1998, ApJ, 504, 1020
Lepri, S. T., & Rivera, Y. J. 2021, ApJ, 912, 51
Lepri, S. T., & Zurbuchen, T. H. 2010, ApJ, 723, L22
Lepri, S. T., Zurbuchen, T. H., Fisk, L. A., et al. 2001, JGR, 106, 29231
McComas, D. J., Bame, S. J., Barker, P., et al. 1998, SSRv, 86, 563
Owens, M. J. 2018, SoPh, 293, 122
Pottasch, S. R. 1963, ApJ, 137, 945
Raymond, J. 1999, SSRv, 87, 55
Raymond, J., Suleiman, R., Van Ballegooijen, A., & Kohl, J. 1997a, in Correlated Phenomena at the Sun, in the Heliosphere and in Geospace, ESA SP-415, ed. A. Wilson (Noordwijk, The Netherlands: European Space Agency), 383
Raymond, J. C., Kohl, J. L., Noci, G., et al. 1997b, SoPh, 175, 645
Raymond, J. C., Fineschi, S., Smith, P. L., et al. 1998, ApJ, 508, 410
Richardson, I. G., & Cane, H. V. 2010, SoPh, 264, 189
Rivera, Y. J., Landi, E., Lepri, S. T., & Gilbert, J. A. 2019, ApJ, 874, 164
Rivera, Y. J., Lepri, S. T., Raymond, J. C., et al. 2021, ApJ, 921, 93
Uzzo, M., Ko, Y.-K., & Raymond, J. C. 2004, ApJ, 603, 760
Uzzo, M., Ko, Y.-K., Raymond, J. C., Wurz, P., & Ipavich, F. M. 2003, ApJ, 585, 1062
von Steiger, R., Schwadron, N. a., Fisk, L. A., et al. 2000, JGR, 105, 27217
Weberg, M. J., Lepri, S. T., & Zurbuchen, T. H. 2015, ApJ, 801, 99
Weberg, M. J., Zurbuchen, T. H., & Lepri, S. T. 2012, AJ, 760, 30
Zurbuchen, T. H., Fisk, L. A., Gloeckler, G., & Von Steiger, R. 2002, GeoRL, 29, 1352
Zurbuchen, T. H., Fisk, L. A., Lepri, S. T., & Von Steiger, R. 2003, in AIP Conf. Proc. 679, Solar Wind 10 (Melville, NY: AIP), 604
Zurbuchen, T. H., & Richardson, I. G. 2006, SSRv, 123, 31
Zurbuchen, T. H., Weberg, M., Steiger, R. V., et al. 2016, ApJ, 826, 10